Distribution of Materials Excavated by the Lunar Crater Bullialdus and Implications for the Geologic History of the Nubium Region

STEFANIE TOMPKINS, CARLÉ M. PIETERS, AND JOHN F. MUSTARD

Department of Geological Sciences, Box 1846, Brown University, Providence, Rhode Island 02912
E-mail: tompkins@pggipl.geo.brown.edu

AND

PATRICK PINET AND SERGE D. CHEVREL

UPR 234, GRGS, Observatoire Midi-Pyrenees, 14 Ave. Edouard Belin, 31055 Toulouse Cedex, France

Previous spectroscopic studies of the lunar crater Bullialdus, located in the Nubium Basin, indicated an unusual stratigraphy of two gabbroic layers overlying a noritic unit. The possible existence of a layered mafic pluton at Bullialdus was suggested. To investigate the geologic context with more detailed spatial information, charge-coupled device (CCD) images of Bullialdus were obtained using eight filters (0.40, 0.56, 0.73, 0.91, 0.95, 0.98, 0.99, and 1.02 μm). A linear mixing model was used to investigate the fractional abundances of spectral end-members chosen from within the multispectral image. Since the reflectance properties of lunar materials over this wavelength range are sensitive to variations in composition and soil maturity, fractional abundance images were used to create a new geologic map of the crater. The spatial relationships of the surface materials confirm the previously inferred stratigraphy, and further reveal the central peaks to exhibit two distinct compositional units: noritic anorthosite and anorthositic norite. Three models for the origin of the observed stratigraphy are considered: Bullialdus has excavated stratigraphic units containing (1) early mare basalt overlying anorthositic–noritic crustal material, (2) part of a layered mafic pluton, and/or (3) part of an impact melt sheet formed by the Nubium Basin impact event. © 1994 Academic Press, Inc.

INTRODUCTION

Much of the history and subsurface structure of the Earth's moon remains a mystery, despite the variety of geologic data that have been collected over the past 30 years. A widely accepted theory for the formation of the lunar crust involves a magma ocean. This magma ocean differentiated, with plagioclase floating to the surface and heavier mafic minerals sinking to the base of the lithosphere (Wood *et al.* 1970; Walker *et al.* 1975). However, study of lunar samples has shown that there may be more than one source of magma involved. Plots of Mg/(Mg + Fe) (Mg* or Mg-number) of mafic minerals against Ca/(Ca + Na + K) ratios in plagioclase of "pristine" lunar samples show three distinct trends: the highly feldspathic ferroan anorthosite suite (FAN), the alkali anorthosites, and the Mg-suite, with consistently high Mg* relative to Ca/(Ca + Na + K) (Warren and Wasson 1977). One suggested modification to the magma ocean theory that allows for these different magma sources invokes layered Mg-suite plutons (similar to that found at the Stillwater Complex, for example) intruding into an already present ferroan anorthosite crust (Raedeke and McCallum 1980). Some evidence of such plutons has been suggested in the distribution of materials around the craters Aristarchus (Lucey *et al.* 1986), Copernicus (Pieters and Wilhelms 1985), Tycho (Hawke *et al.* 1986), and Bullialdus (Pieters 1991).

Pieters (1986) conducted a survey of a number of simple and complex impact craters on the lunar nearside. The mafic mineralogy of the Moon's surface can be distinguished remotely with near infrared spectroscopy based on the shape and position of various absorption bands. This particular study melded remote reflectance spectroscopy with impact crater theories to determine the composition of material beneath the lunar regolith. As demonstrated in surveys of terrestrial impact craters, the central peaks found in complex craters (20–100 km in diameter) are formed of material uplifted from beneath the surface. Scaling relationships indicate that the preimpact depth of central peak material can be related to the final crater diameter, and that this is the deepest material uplifted by an impact (Melosh 1989, Grieve *et al.* 1991). By combining spectral data with these kinds of impact crater relationships, Pieters (1986, 1993) provided a partial map of

261

crustal material down to 5–15 km depth. The general trend indicated an uppermost layer of noritic breccia, primarily seen in smaller craters without central peaks. At large craters, noritic material was also commonly observed in the uppermost crust. Beneath this layer, greater diversity was observed, including anorthosite, troctolite, or gabbro.

Exceptions were at the craters Aristarchus (gabbro and troctolite in the upper layer) (Lucey et al. 1986), Tycho (all gabbro) (Hawke et al. 1986), and Bullialdus (gabbroic upper layer overlying a noritic lower unit) (Pieters 1986). Because of the unusual stratigraphy at Bullialdus, further analyses of high-spectral-resolution telescopic data were conducted by Pieters (1991), and high-spatial-resolution multispectral CCD images were acquired. The discussion below focuses on the analysis of the CCD data and a further evaluation of the crustal stratigraphy near Bullialdus and of its possible origins. Spectral mixture modeling is used to evaluate the relative abundance and spatial distribution of spectrally distinct materials at Bullialdus. These end-member materials are then related to various lithologic units and examined in geologic context in order to derive a revised stratigraphy for this region of the Nubium Basin.

A description of Bullialdus' geologic setting is given in the next section, followed by a discussion of the data and the analytical methods that were applied. Finally, the results are presented, and several models for the emplacement of the Bullialdus materials are considered.

BACKGROUND

Regional Geology

Bullialdus is an Eratosthenian-age impact crater located along the western edge of Mare Nubium (22 S, 23 W), approximately 60 km away from the eastern edge of Mare Humorum (Fig. 1). The Nubium and Humorum Basins are located in the southwestern quadrant of the nearside of the moon, at the southern end of Oceanus Procellarum. The Humorum Basin is Nectarian in age, and approximately 460 km in diameter. Mare Nubium is in a larger, pre-Nectarian, more irregularly shaped region made up of one or more multiring basins, directly east of Humorum.

The preimpact stratigraphy within the Nubium Basin is expected to contain deposits of the Vitello Formation (Humorum ejecta), and perhaps a variety of other impact-related lithologies and basalt flows. The thickness of the ejecta deposited by the Humorum Basin event at the location of the Bullialdus impact can be estimated at ~500 m (McGetchin et al. 1973). A thin layer of Imbrium ejecta might also be expected. The uppermost layer consists of Upper Imbrian mare basalt whose thickness was calculated to be 250–500 m (DeHon 1977).

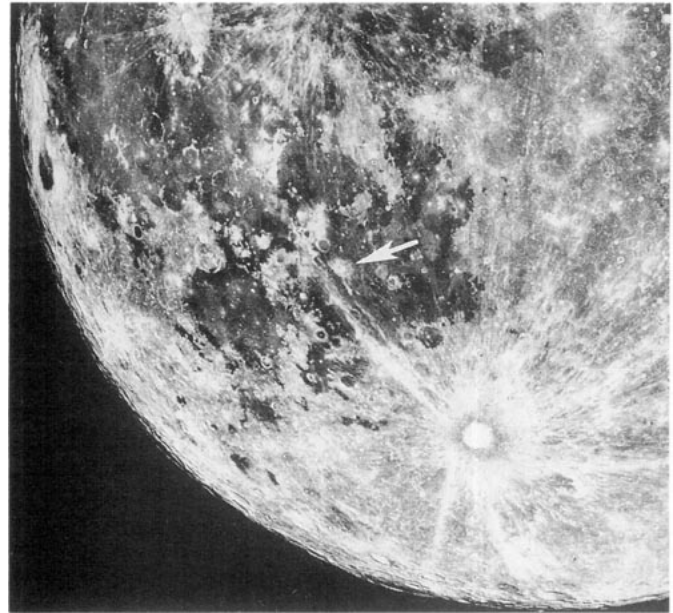At 61 km in diameter, Bullialdus is a typical complex

FIG. 1. Photo of SW portion of lunar nearside, with Bullialdus indicated by an arrow.

crater with multiple central peaks and a predominantly hummocky floor (Figs. 2 and 3). According to previous geologic studies (Trask and Titley 1966), a graben runs NE–SW through the central peaks. Bullialdus' walls are terraced, with slumping evident in the west and northeast. The western wall and rim of the crater are characterized by a higher albedo, which corresponds to a ray of the crater Tycho. The crater ejecta is also typical for Bullialdus's size, with continuous ejecta surrounding the crater to approximately one-half crater radius, grading into a series of radial ridges and grooves, and then into a zone of secondary craters. Basalt flows have embayed the ejecta deposits from the northwest, to within one crater radius of the rim.

Mineralogy

The telescopic near-infrared spectra of the Bullialdus central peaks, walls, and rim are shown in Fig. 4 (from Pieters 1991). The criteria used to determine composition are primarily the strength, shape, and position of absorption bands and albedo. The position and shape of the strong mafic absorption near 1 μm identify the dominant mafic mineral present. In general, band strength is directly proportional to the abundance of ferrous minerals. However, band strength can be weakened by the presence of strongly absorbing species, or processes such as space weathering. Since plagioclase has a high reflectance but only minor absorptions in this wavelength region, its presence is typically inferred from relative albedo.

The classification scheme of Stöffler et al. (1980) for

lunar highland rocks has commonly been used to define general lithologic boundaries in analyses of near IR reflectance spectra. As illustrated in Fig. 5, the classification for gabbroic–noritic rocks is based on the ternary system of plagioclase, orthopyroxene, and clinopyroxene. A first order classification can be based solely on the type of pyroxene identified, placing a material in the noritic (orthopyroxene) half of the triangle or the gabbroic (clinopyroxene) half. At Bullialdus, the absorption band of the central peaks' spectrum has a minimum at 0.93 μm, indicating low-Ca pyroxene to be the dominant mafic component (Adams 1974) (see Fig. 4). In accordance with the diagram in Fig. 5, the presence of low-Ca pyroxene led to a classification of the central peaks as noritic (Pieters 1991). The absorption band is strong and symmetric in shape, which was interpreted to indicate a relatively crystalline (versus brecciated or glass-rich) material.

Absorptions observed in the wall spectra have minima at 0.98 μm, indicating the dominance of high-Ca pyroxene. The presence of high-Ca pyroxene suggests a gabbroic or basaltic rock (Fig. 5). The distinction between a gabbro or basalt, which is primarily one of texture in hand samples, may not be apparent in their spectra. Therefore, unless stated otherwise, the term "gabbroic" in this paper simply refers to rocks with a relatively high abundance
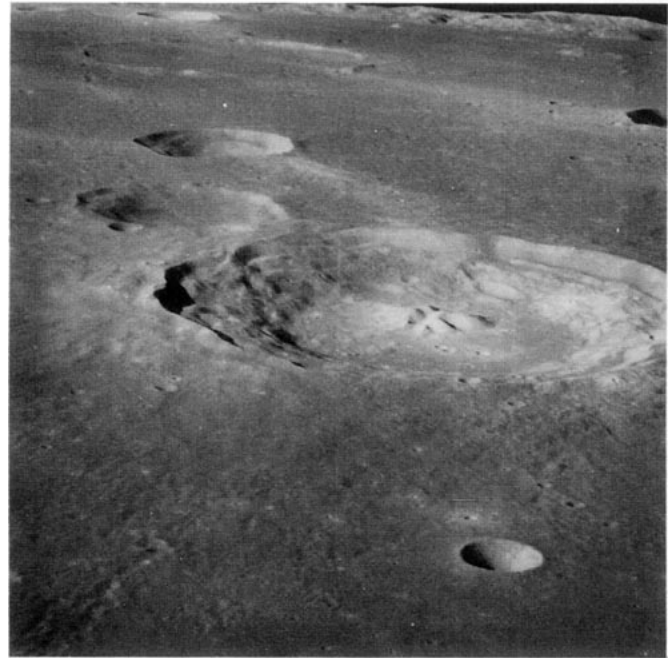

FIG. 3. Oblique Apollo 16 photograph (AS16-119-19094) of Bullialdus taken from the north (view is towards the south).

FIG. 2. Mosaic of two Lunar Orbiter photographs of Bullialdus (IV 125 H-1 and IV 125 H-2), with north indicated by the arrow. The two photographs were digitally scanned and then filtered using a fast Fourier transform algorithm (explained by Sunshine *et al.* 1994). The filtering process removes the line between the two images and between the original Lunar Orbiter framelets.

of high-Ca pyroxene, and does not by itself suggest an intrusive or extrusive origin for those rocks.

The crater rim spectra indicate material that is also gabbroic, but with two differences that distinguish it from the wall material. The 1-μm absorption bands are broader and they are centered at slightly longer wavelengths, indicating the presence of an additional mafic component such as Fe-bearing glass or olivine. If the additional component is glass, it may represent impact melt along Bullialdus' rim. Impact melt has been observed along the rims of many lunar impact craters (Hawke and Head 1977). This rim unit was inferred to have been the uppermost of the layers excavated by the Bullialdus impact, overlying the other gabbroic unit. The two gabbros in turn lay above the noritic unit excavated by the central peaks (Pieters 1991).

DATA ACQUISITION AND REDUCTION

CCD images with high-dynamic range (16-bit intensities) were obtained with a 576 × 384 pixel-array Thomson CCD camera mounted on the 2-m telescope (F/D = 25) of the Pic du Midi Observatory. The observations were carried out in the October 1989 full-moon period, under less than 2° phase angle values and with excellent atmospheric stability conditions. The optical configuration corresponds to a theoretical spatial resolution of 0.2 km/pixel (Pinet *et al.* 1992). Seeing conditions were approximated
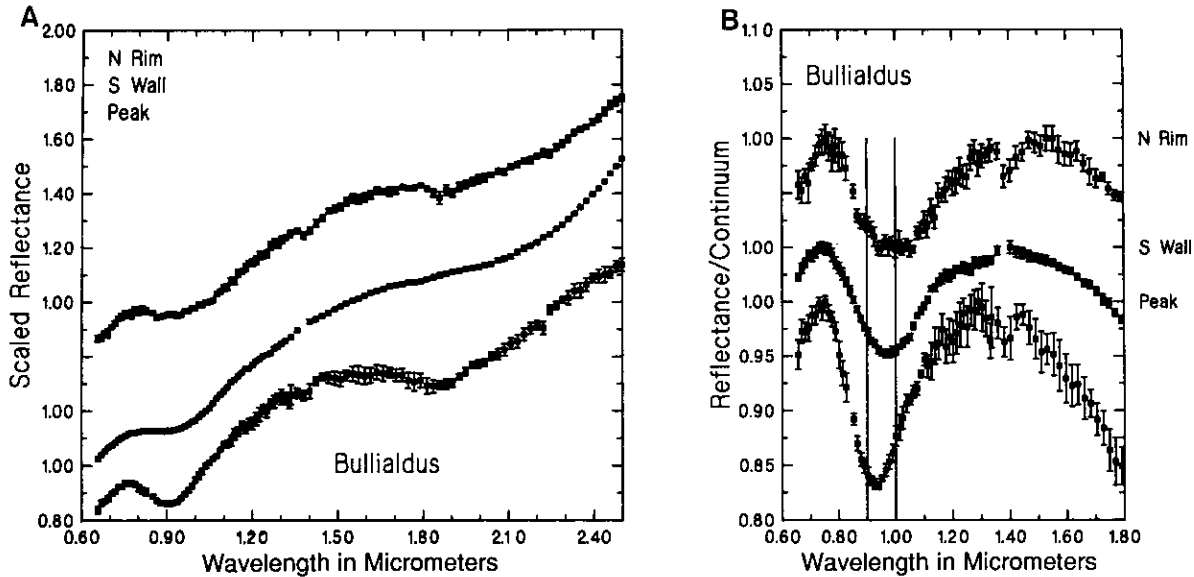
FIG. 4. Telescopic spectra of Bullialdus' rim, wall, and central peaks (from Pieters 1991). Spectra in 4A are relative to sun, and in 4B are continuum removed. The central peak absorption band, with a minimum near 0.93 μm, indicates the presence of low-Ca pyroxene. The wall and rim have absorptions near 0.98 μm, indicating a high-Ca pyroxene component.

to be 0.5 arcsec, which corresponds to approximately 0.8 km. Ten spectral images were taken at 0.40, 0.56, 0.73, 0.91, 0.95, 0.97, 0.98, 0.99, 1.02, and 1.05 μm with high spectral resolution (wavelength/bandpass = $\Delta\lambda/\lambda \sim$ 100). Images using all 10 bands were processed with stan-
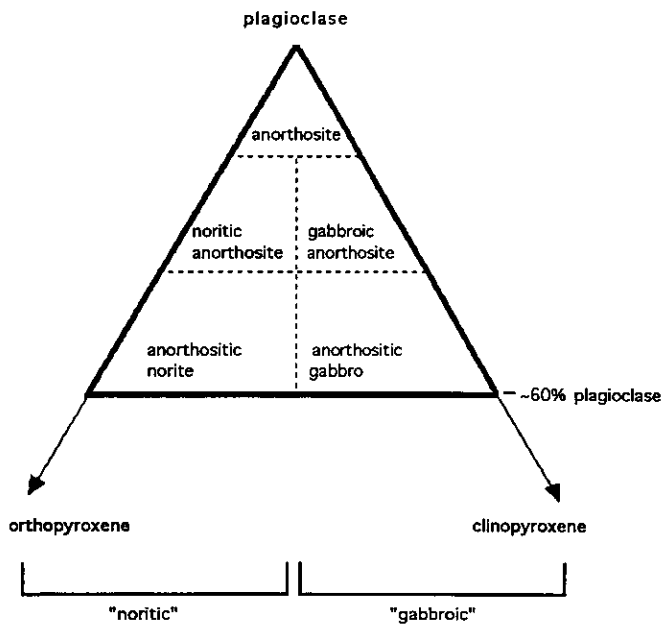

FIG. 5. Ternary diagram after Stöffler *et al.* (1980), showing the classification of lunar highland gabbroic–noritic rocks as a function of their plagioclase, orthopyroxene, and clinopyroxene abundance (pyroxene/olivine is assumed to be >1). The lower boundary indicates approximately 40% pyroxene.

dard flatfield and offset corrections; however, data acquired with the 0.97 and 1.05 μm filters show spectral anomalies and have not been used in the analysis discussed here. Previous evaluations (Chevrel *et al.* 1991, Pinet *et al.* 1993) using a data set obtained with the same instrumentation for the crater Copernicus have determined, however, that this new type of data are a generally consistent (within 1–2% standard deviation) in terms of overall continuum slope and absorption features with earlier near-infrared spectra available for particular spots.

For Bullialdus, images taken at 0.73 μm and longer wavelengths were calibrated to near-infrared telescopic spectra (Pieters 1991). The telescopic spectra were first resampled through the French CCD filter bandpasses, and corrected to absolute reflectance using the relationship

$$\frac{\text{telescopic}}{\text{Apollo 16}} \times \frac{\text{Apollo 16}}{\text{halon}} \sim \frac{\text{telescopic}}{\text{sun}},$$

where Apollo 16 measurements relative to halon were measured in the laboratory, and are approximately equivalent to absolute reflectance. Telescopic spectra relative to Apollo 16 were calculated from reflectance measurements of the Apollo 16 landing site taken during the same observing period as the Bullialdus spectra.

The CCD reflectances were calibrated to their respective telescopic values using an empirical line method (e.g., Elvidge 1988), where gain and offset values were derived for each CCD band based on a least-squares fit to the two data sets. Images obtained at 0.40 and 0.56 μm were calibrated in the same way using Galileo Solid State Im-
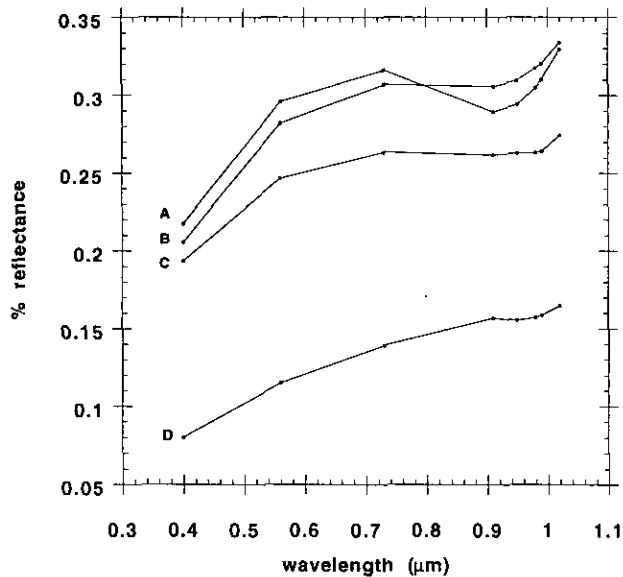
FIG. 6. CCD spectra (relative to sun) of the four spectral end-members used in the mixture analysis. The central peaks are represented by two different compositions, as seen in the different relative strengths of their absorption bands. The difference between the wall and ejecta end-members is interpreted to be one of soil maturity.

aging (SSI) system data (Pieters *et al.*, submitted for publication), but the accuracy of these spectral calibrations may be lower due to the lower precision and spatial resolution for the SSI instrument. The calibrated (i.e., absolute reflectance) CCD spectra for four lithologic units in the Bullialdus images are shown in Fig. 6. These four units were used as end-members in the spectral mixture analysis and are discussed in more detail below.

IMAGE ANALYSIS

Spectral Mixture Modeling

An image-based, linear spectral mixing model was used on the CCD data to evaluate the distribution of spectroscopically distinct materials across the crater (Adams *et al.* 1993). The underlying assumption of spectral mixture analysis is that each pixel spectrum incorporates a linear combination of end-member reflectance spectra. These end-members can either be image end-members, selected from the scene itself (as in the case presented here), or reference end-members, taken directly from a spectral library. In the most general approach, the spectral variability of a scene can be modeled as a linear combination of a small number of end-members whose spectral properties are combined in a least-squares mixing algorithm to provide the optimal fit for each pixel spectrum within the image. Each pixel can be represented by the fractional amount of each end-member required to best fit the actual pixel spectrum, with the sum of the fractions constrained to 1.0. The fractional abundances of the selected end-

members within each pixel are represented visually in fraction images. There is a fraction image for each end-member, which shows the relative abundance of that end-member across the scene.

While mathematically the total number of end-members may not exceed the number of bands plus one, the maximum number of end-members presumes variables that are linearly independent. We know that lunar spectra are highly correlated channel to channel, and therefore do not expect to be able to detect as many end-members as are technically possible. The Bullialdus image analysis was begun with the selection of four spectrally distinct image end-members. Image end-members were refined using ratio images, geologic maps, and photographs (Apollo 16 oblique and Lunar Orbiter) to define physically meaningful, spectrally distinct areas to represent initial end-members. These end-member components were explored further using subsets of the image, or by selectively omitting spectral channels.

The validity of a solution using a particular group of end-members to characterize a scene is difficult to quantify. The simplest measure is to reduce the root-mean-square error to a statistically significant limit (typically the noise level of the system) through a continual refinement of end-member selection (number and location). This is generally done through a logical trial-and-error process, although more objective methods are currently being explored (Tompkins *et al.* 1993). Most importantly, however, fraction images must make physical sense as well as satisfy basic statistical requirements. The fraction values themselves should lie between 0 and 1, although small deviations outside this range are allowed. (Negative or "superpositive" fraction values often serve to indicate areas that are not explained by the simple linear system assumed by the mixing model.) Ultimately, spatial coherency and geologic context play large roles in judging the validity of spectral mixing model results.

A low albedo, spectrally neutral end-member ("shade") is commonly used to model specific variations in spectral properties within an image. These variations arise from illumination (such as shadows) or simple scaling, and are not related to composition. Because the Bullialdus CCD images were acquired at small phase angles (1 to 2°), identification of a "shade" end-member was not necessary.

Physical Interpretation of Fraction Images

Four end-members were ultimately chosen to model the Bullialdus image. The end-member fraction images are presented in Fig. 7. Individual fraction images are shown both superimposed on a Lunar Orbiter IV mosaic of the same area to provide a spatial context (Figs. 7A–D), and without the Lunar Orbiter base map in Figs. 8A–D. The variance image, shown in Fig. 8E, displays the root-
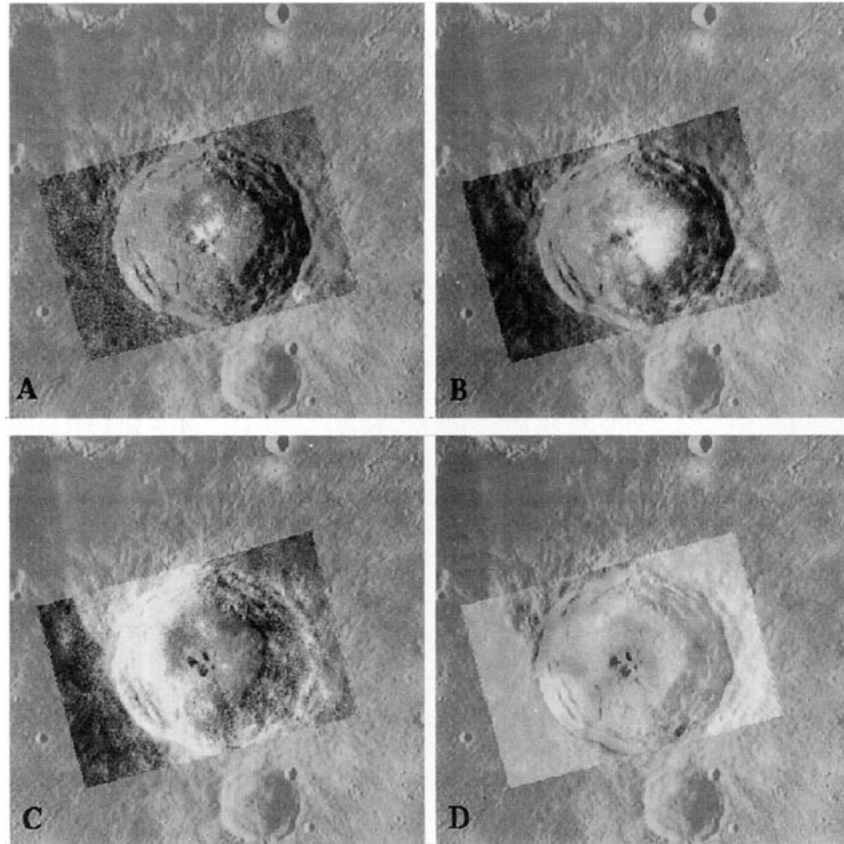
FIG. 7. Fraction images of Bullialdus spectral end-members, superimposed on a Lunar Orbiter photo mosaic (Fig. 2). 7A is the fraction for the northern central peaks, 7B for the southern central peaks, 7C for the wall material, and 7D for the ejecta.

mean-square error, or the difference between the true reflectance values and the values predicted by the mixing model for each pixel. The average standard deviation for the image was less than 2%. The locations of the end-members whose spectra (Fig. 6) were used in the mixture model are marked on the fraction images. A discussion of the end-members is given below.

Central Peaks. The mixture analysis results show the central peaks of Bullialdus to be composed of two distinct lithologies (Figs. 7A and 7B, 8A and 8B). The boundary between these units coincides with the narrow graben running through the center of the crater that had been mapped in earlier studies (Trask and Titley 1966), although this feature is not visible in either the CCD or Lunar Orbiter images used for this study. The most sharply defined, spatially coherent end-member is limited to the northern portion of the central peaks (Fig. 7A). The spectrum of this end-member (Fig. 6) is similar but not equivalent to the telescopic noritic spectrum (which was a composite of the entire central peak area), with a high albedo and a strong absorption band centered near 0.93 μm. The remainder of the peaks and part of the

floor (End-member B, Fig. 7B and 8B) are shown to be a distinctly different unit, with a notably shallower 1-μm absorption but a generally similar albedo. The separation of the central peaks into two compositions requires a refinement of their initial classification as noritic rocks. Based on the position of the absorptions near 0.93 μm, both units are interpreted to have low-Ca pyroxene as the dominant mafic component, and the shallower band in End-member B can be attributed to either a chemical difference (e.g., a lower abundance of pyroxene relative to plagioclase than End-member A) or a physical difference (e.g., higher degree of brecciation corresponding to smaller particle sizes, or a higher degree of maturity) that serves to weaken the strength of the absorption band. The latter option is less likely because the physical processes that might weaken a band would also be expected to change the albedo of the spectrum, and in this case, the two peak units do not have significant differences in albedo. In addition, there is no apparent difference in the morphology of the two units, which might be expected if they varied in maturity or degree of brecciation. The difference between the two units is therefore interpreted
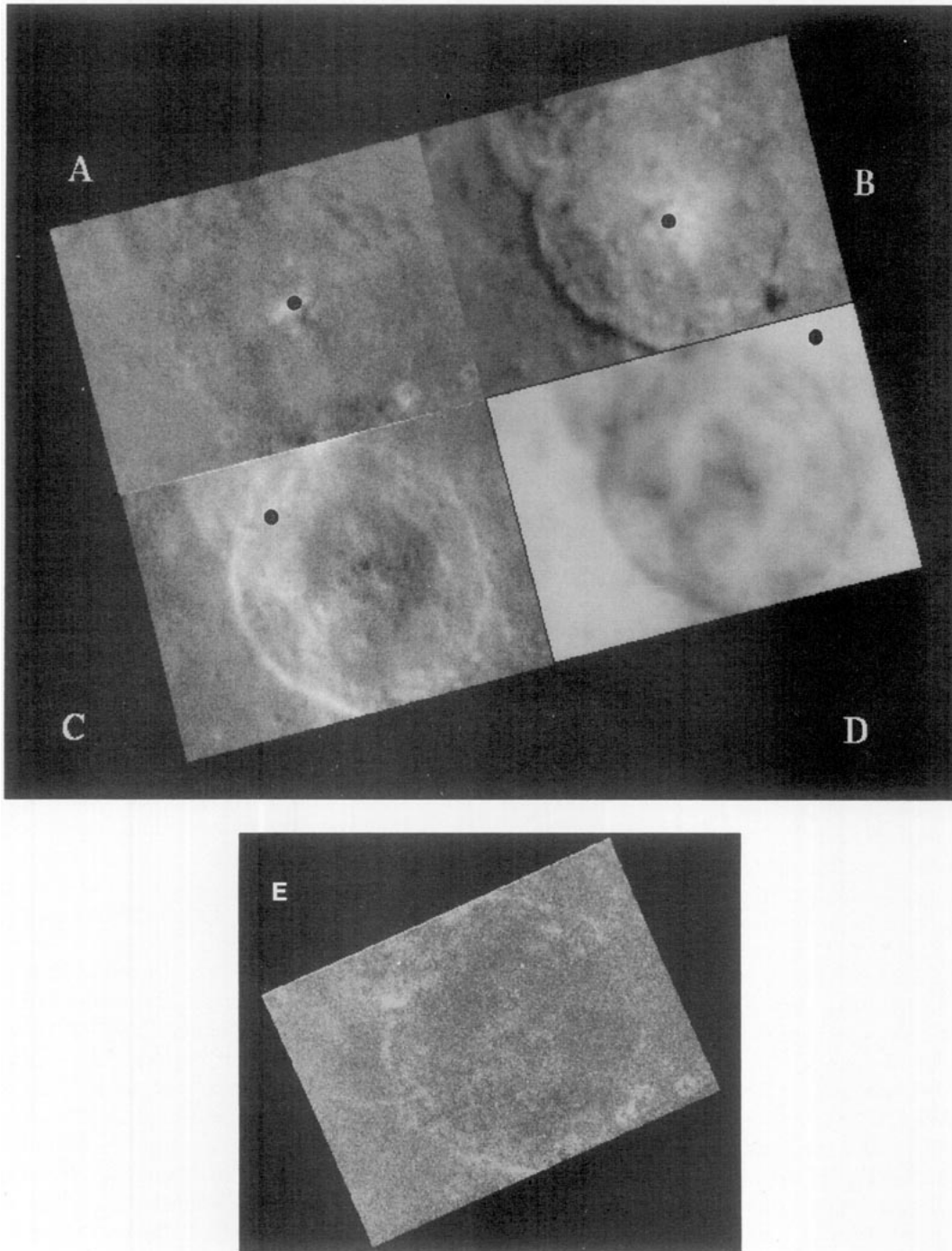
FIG. 8. A–D (above) are the fraction images without the Lunar Orbiter base image, arranged as for Fig. 7. The small black circles indicate the approximate locations of the image end-members. E (below) is the variance image (illustrating root-mean-square error of the fit for each pixel).

to be a function of the relative abundances of pyroxene and plagioclase. The relation between the two units is comparable, in a relative sense, to that between anorthositic norite (End-member A) and noritic anorthosite (End-member B) on the ternary diagram in Fig. 5.

Floor. The crater floor is comprised of a complex mixture of impact related lithologies (ejecta, melt, etc.) and later deposits (mass wasting from walls and peaks). Spectrally, floor material does not represent a simple linear mixing scenario. For example, the hummocky floor mate-

rial surrounding the southern central peaks appears to contain a large fraction of the southern peaks end-member (Figures 7B and 8B). However, a closer examination of the spectra of the floor material reveals that it is not directly associated with any one of the mixture model end-members. Shown in Fig. 9 are spectra from various locations within and around the crater. These are arranged to show the changes in the spectra between the center and the rims (Fig. 9B and 9C). The reason the floor material appears to have a high relative abundance in the End-member B fraction image is that the pixel spectra for the area are best fit mathematically in the mixing model by more than 100% of End-member B, and small negative amounts of the other end-members. It is possible that the floor comprises large amounts of End-member B. It is more likely, however, that the floor is associated with End-member B because it is relatively bright, and with End-members C and D because the spectral slope and 1 μm absorption feature characteristics are more closely associated with those units (see below). This association with multiple end-members is not surprising, as the crater floor is expected to be a mixture. Furthermore, the physically unrealistic combination of end-members to describe the floor material is an indication that the mixture of materials is more complex than can be explained by a simple linear model.

Crater Walls and Ejecta. The small difference in absorption features observed previously between the wall and rim (derived from near-infrared spectra) cannot be detected within the spectral range of the CCD images. Instead, the two end-members that describe the crater walls and ejecta appear to be strongly linked to lunar weathering. End-member C includes both wall and rim material (Fig. 7C and 8C). End-member D is from the low-albedo ejecta material surrounding the crater, and appears in varying amounts within the crater as well (Fig. 7D and 8D). Both end-member spectra have a long wavelength 1-μm absorption band that indicates the presence of high-Ca pyroxene, but they differ in spectral slope and albedo. End-member D is darker and has a redder slope than End-member C (Figure 6). Since characteristics of soil maturation include a decrease in albedo and an increase in slope (e.g., Pieters 1993), End-member D appears to represent relatively mature, well developed gabbroic soils, while End-member C represents relatively immature material of the same composition.

The spatial distribution of End-members C and D supports the conjecture that maturity is the primary difference between the two. Areas where End-member D is abundant are expected to have the most mature materials (low-lying flat areas, for example). Furthermore, as shown in Fig. 7C and 8C (End-member C), there is a clear asymmetry between the western and eastern sides of the wall, which may be partly explained by the presence along the

western edge of a Tycho ray. The ray material is younger than Bullialdus, and the area that has been affected by the ray has a higher albedo than adjacent areas. Tycho Crater is also gabbroic in composition (Hawke *et al.* 1986), so there may be no other compositional distinction between the ray material and the rest of the Bullialdus wall.

In order to understand the interaction of maturity and composition better, End-members C and D were initially divided into three end-members: fresh, intermediate, and mature gabbroic material. The statistical improvement to the rms error using an additional end-member was negligible, but the spatial distribution of the three units had a clear physical basis. The fresh material was confined to the Tycho Ray and steep slopes along the terraced walls. Intermediate material included parts of the crater floor and local topographic lows along the walls. The mature material fraction image remained generally similar to that shown in Figure 7D and 8D. While this particular solution made clear the link between maturity and the different end-members, the final result did not seem to require a separate end-member for the intermediate gabbroic soils, as they could be modeled as a mixture between fresh and mature gabbroic material. It should be noted, however, that there is no reason to expect the maturation process to be described by a linear mixing model. The simplification is reasonable for this analysis, because the model results still provide an indication of the relative (rather than absolute) maturity and abundance of gabbroic materials within the image. For quantitative estimates of maturity, the mixing algorithm would have to be linked to a physically realistic model relating lunar weathering to the alteration of spectra.

The spectral mixture model used in this analysis supports the overall stratigraphy originally interpreted from near-infrared spectra (Pieters 1986, 1991), and confirms a symmetric spatial distribution for the gabbroic units. However, without higher-spectral-resolution data with broader spectral coverage, the previously identified compositional differences between gabbroic units in the crater wall and rim cannot be distinguished. This compositional information, studied in conjunction with a Lunar Orbiter image to show fine details and general morphology, still gives a reasonably comprehensive picture of Bullialdus. Based on the fraction images, the distribution of lithologic units in and around Bullialdus is presented in map form in Fig. 10. In this map, the gabbroic material composing the walls and ejecta is shown at three different stages of maturity: fresh (where the Tycho ray crosses the crater), intermediate (the remainder of the walls), and mature (the ejecta material). Additional distinct lithologic units are the two central peaks compositions, which indicate a compositional boundary between anorthositic norite and noritic anorthosite. Finally, the floor material is expected to
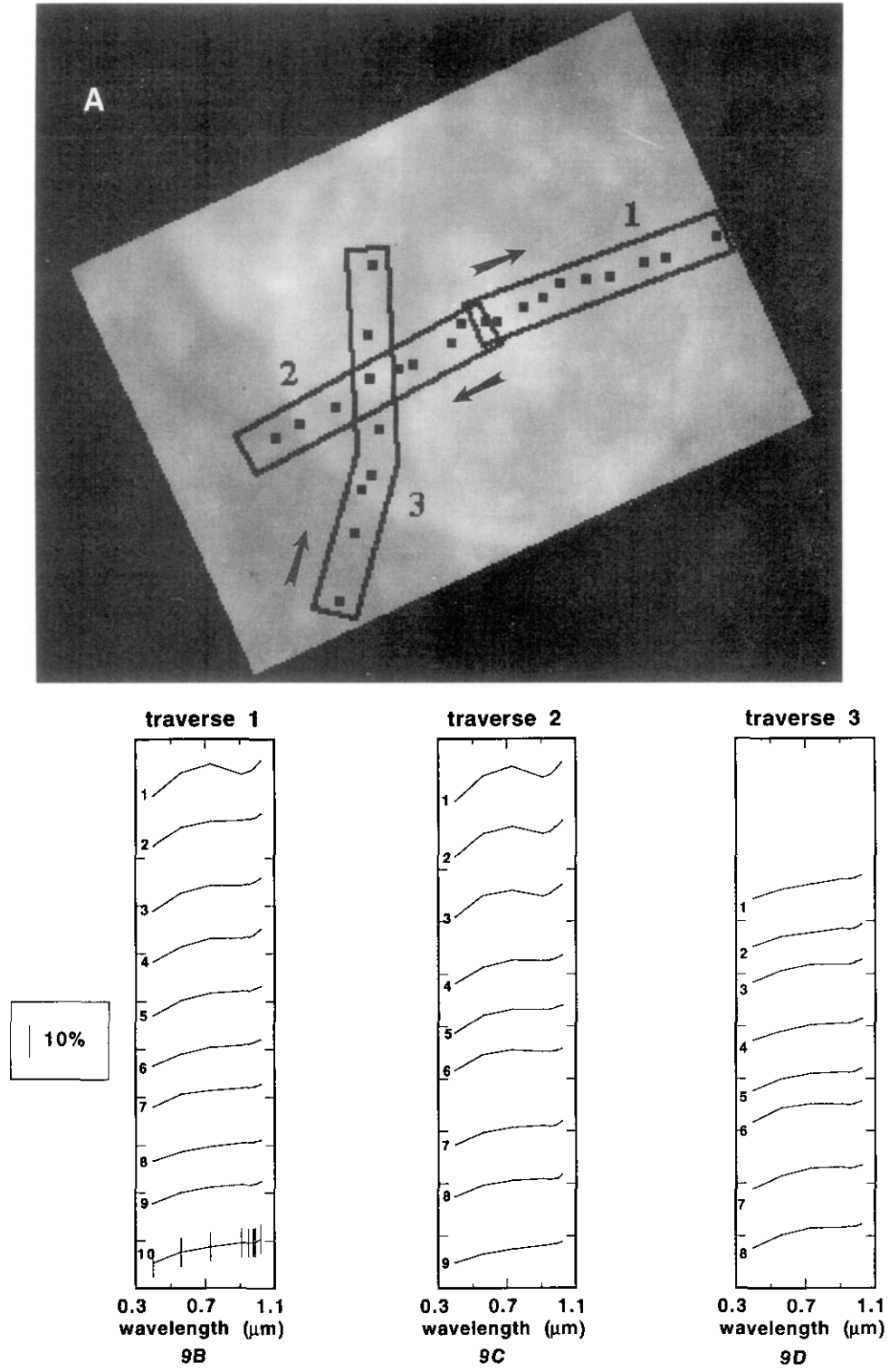
FIG. 9.   CCD spectra of cross-crater traverses. A shows the locations of the three traverses, with arrows indicating the order in which the spectra were taken. B, C, and D are the spectra of the 1-pixel boxes as indicated, numbered in the order they were taken. Spectra are relative to sun, but have been offset for clarity: the tick marks on the vertical axes represent the 0% reflectance point for the next spectrum up. Shown in the legend is a bar indicating 10% reflectance for spectra. The standard deviation is less than 1% for each spectrum. Note that the eastern and western traverses share a common starting point.

anorthositic norite
noritic anorthosite
floor material
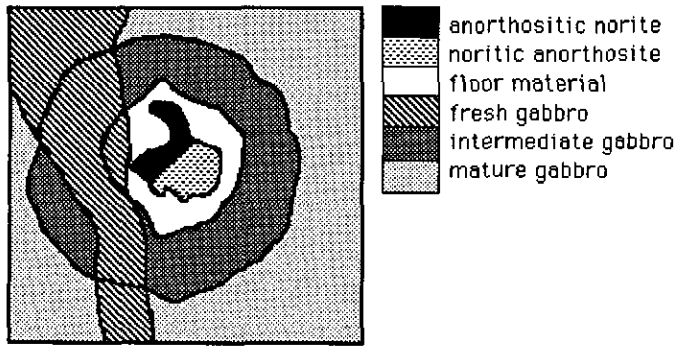fresh gabbro
intermediate gabbro
mature gabbro

FIG. 10. Distribution of lithologic end-members within Bullialdus, based on the fraction images.

consist of a mixture of materials, including run-off from the walls and peaks and impact melt.

DISCUSSION

The geologic relationships of material excavated and exposed by Bullialdus must be considered in the context of the formation and evolution of the Nubium Basin. The Nubium Basin has been modeled in two different ways. According to DeHon (1977) it is a series of four overlapping multiring basins. Of these, the "Western Nubium Basin" is the largest (~410 km in diameter) and oldest. In this context, Bullialdus could sit just within and partly overlapping its inner ring. On the other hand, Wilhelms (1987; 1993, personal communication) considers Nubium to be a single basin (~600 km in diameter), which intersects the younger Humorum Basin to the west. Again, Bullialdus is likely to be located near an inner ring, if one exists. The original depth of the basin is unknown, but is estimated at 5 km or less, based on the depths of younger and better studied basins such as Orientale (e.g., Head 1974) and on gravitational modeling, which indicates that the older basins are somewhat shallower than the younger ones (e.g., Bratt et al. 1985). Current basin fill is expected to consist of impact melt, ejecta from subsequent basin-forming impacts, and basalt. The major basin-forming events that are likely to have affected the Nubium Basin are Humorum and Imbrium (Wilhelms 1987).

Based on impact crater relationships and the surface lithologies described in Fig. 10, a preimpact stratigraphy for Bullialdus has been inferred. Summarized in Table I are the observed units and their preimpact positions, from top to bottom. Unit 1 is derived from photogeologic analysis, or general geologic history; units 2–4 have been identified using spectroscopic data. The order does not imply that successive units are contiguous, however. For example, Humorum basin ejecta are expected to be present, although they are not detected at Bullialdus. It may be

present in the preimpact stratigraphic column, however, either as a discrete layer that has not been exposed by the Bullialdus impact, or as material that has been excavated and removed, or mixed into the gabbroic material now seen in the crater walls and rim. In the latter case, since Humorum material is interpreted as a noritic feldspathic breccia (Johnson et al. 1973, Pieters et al. 1975, Lucey et al. 1991), it would serve principally as a brightening agent if mixed with gabbroic material.

The central peak units are believed to have been uplifted from a depth of 6 km or greater (e.g., Melosh 1989; Cintala and Grieve 1993). Because of the uncertainty in both the depth of the Nubium Basin and the depth of origin of the peaks, the peaks could have come either from within the Nubium Basin, or from beneath it. The actual relationship between these two noritic units (4a and 4b, Table I) merits a closer evaluation, because they are believed to have been uplifted from the same depth, but are compositionally different. Several stratigraphic relationships are possible. For instance, the compositional difference could result from a laterally heterogeneous layer. However, the fact that a graben occurs along the compositional contact (Trask and Titley 1966) suggests that a structural relationship, such as two layers faulted at depth or dipping (perhaps related to Nubium Basin formation or structure), or some fortuitous combination of thin and thick layers, might better explain the observed difference between the central peaks.

The spectral mixture model results show a clear pattern in the distribution of Bullialdus' surface material that can be translated to a stratigraphic sequence, as summarized above. Combined with what is known about the regional geology, this evidence can be interpreted in several ways. Outlined below are three general models for the emplacement of the different mafic layers excavated by Bullialdus. Variations on these hypotheses are of course possible, as is some combination of two or more of the models.

Model 1: Early Basalt (Fig. 11A)

In this model, the high-Ca pyroxene material in the crater walls is from earlier basalt flows. This model had not been considered previously because the thickness of the Upper Imbrian basalt in the Nubium Basin had been estimated at 250–500 m (DeHon 1977). This thin layer was not expected to contribute substantially to the volume of the excavated material, since other craters of similar size and geologic setting to Bullialdus (e.g., Copernicus and Lansburg) with a similar thin mare fill exhibit no high-Ca pyroxene signature at all (Pieters 1986; 1993). However, the basalt thickness estimate is accomplished by measuring flooded crater rims, and is thus only an estimate of the thickness from the present surface to the

TABLE I

Lithologic Units Inferred at Bullialdus, Listed in Stratigraphic Order, from the Surface (Unit 1) to 6+ km Depth (Unit 4)

Unit	Rock type	Mineralogy	Current location	Preimpact location
1	Basalt		Surface layer of Mare Nubium, outside of Bullialdus' continuous ejecta	Uppermost layer, 250–500 m thick[a]
2	Gabbro or basalt	Plagioclase, high-Ca pyroxene (plus Fe-bearing glass or olivine)	Crater rim (may include impact melt)	Depth >500 m, thickness unknown
3	Gabbro or basalt	Plagioclase, high-Ca pyroxene	Crater walls	Depth and thickness unknown
4A	Anorthositic norite	Plagioclase, low-Ca pyroxene	Northern central peaks	Depth of 6+ km, Thickness unknown[b]
4B	Noritic anorthosite	Plagioclase, low-Ca pyroxene (less pyroxene than Unit 4A)	Southern central peaks	same as 4A

Note. In addition to units noted here, ejecta from other basin forming events such as Humorum are expected to be present in varying amounts (between Units 1 and 2, for example). Compositional interpretations of different units are derived from photogeology (Unit 1: *Trask and Titley* 1966) and near-infrared spectroscopy (Units 2, 3, and 4: *Pieters* 1991), as well as the CCD spectra as explained in the text (Units 4A and 4B).

[a] DeHon (1977).
[b] Melosh (1989).

most recent cratered surface. It is possible that the Nubium Basin has been flooded with basalt in multiple volcanic episodes. In this scenario, sufficient time elapses after the penultimate flow for its surface to become cratered, and the Imbrian flows flood those craters. The crater rims measured by DeHon are therefore formed on older basaltic material. Thus the thicknesses of only the youngest basalt flow thicknesses in the area have been measured, and the Nubium Basin is almost entirely filled with mare basalt of different ages. This model is supported by gravitational modeling (Bratt *et al.* 1985), which indicates 1 km as the minimum thickness for basaltic-density material that may be present near Bullialdus. The relatively high albedo of Bullialdus' walls can be attributed to recent surface processes (e.g., run-off from the terraces exposing fresher material) or as a characteristic of the pre-impact material (e.g., mixing of the basalt with feldspathic ejecta from other basin-forming impacts).

The noritic central peaks units in this model are basement material uplifted from beneath the Nubium Basin floor. The compositional boundary within the central peaks could be a manifestation of a preexisting fault within the basin.

Model 2: Igneous Intrusion (Fig. 11B)

In this scenario, the mafic layers represent part of a layered mafic pluton, whose position must be constrained both spatially and temporally. The pluton could have been emplaced prior to the Nubium Basin impact, but must have survived the basin forming event(s) that followed. If emplaced subsequent to the basin formation, it must be located at a shallow enough depth to be excavated by Bullialdus. In this scenario, magma intruded into the crust

beneath the Nubium Basin floor, differentiated to form the gabbroic layers, and possibly the noritic layers as well. Constraints on this model come from the structure of the Nubium Basin itself. The location of the inner ring is not clear, but analogy to other basins indicates that Bullialdus may be very near or even directly above an inner ring. The depth to the floor between the inner and outer rings should be much less than the depth to the central basin floor, and would allow the pluton to intrude to relatively shallow depths. It is also possible that the pluton postdates any Humorum deposits and early volcanic activity. Magma would have intruded into these deposits above the Nubium Basin floor, although there is no evidence of surface deformation that might accompany a shallow intrusion.

Model 3: Cooled Impact Melt Sheet (Fig. 11C)

The third scenario is the most controversial, due to different interpretations of the formation and behavior of impact melt sheets in lunar basin-scale impacts. Thick layers of impact melt in lunar basins have not been directly observed, but the existence of such layers has been suggested at least for the Orientale Basin (Head 1974). In Model 3, Bullialdus has tapped an impact melt sheet that resulted from the formation of the Nubium Basin.

Analogy to the Sudbury Igneous Complex (SIC) suggests a number of intriguing possibilities. For example, it has been suggested (e.g., Grieve *et al.* 1991) that the SIC formed through differentiation of a thick impact melt sheet. Using a conservative estimate of Nubium Basin diameter of 410 km (DeHon 1979), the volume of impact melt from basin formation can be calculated to be ~70,000 km^3 from relationships presented by Lange and Ahrens
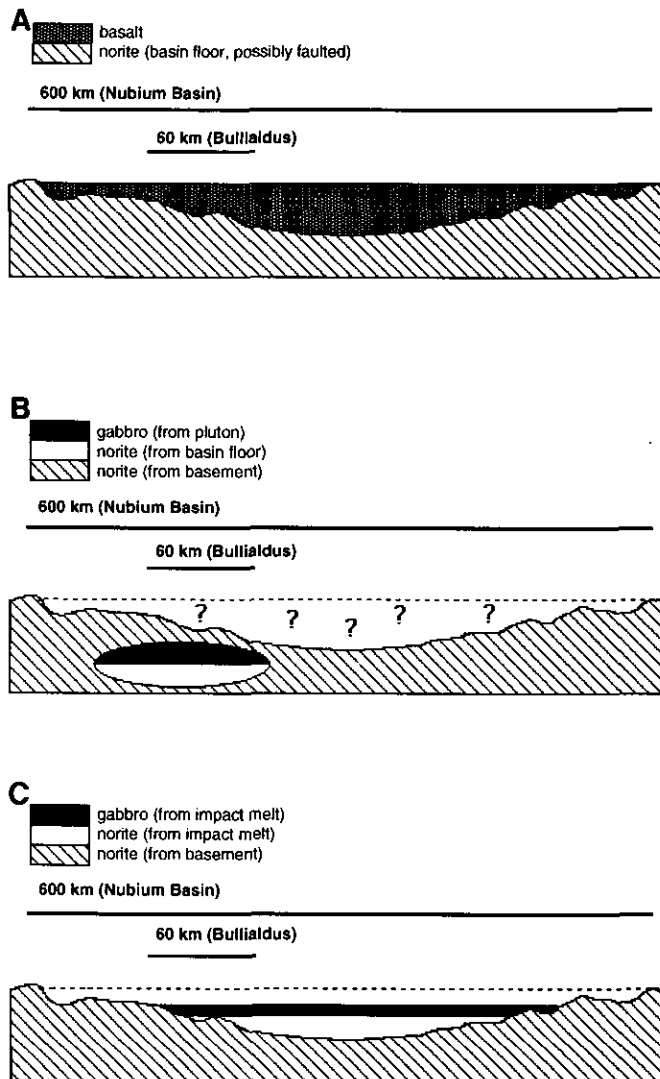
FIG. 11. Schematic cross-sections to illustrate each emplacement model discussed in the text. The 600 km basin is Nubium, and is shown prior to the Bullialdus impact. The 60-km scale bar indicates approximately where the Bullialdus impact would be, although its exact relationship with respect to the structural features of the Nubium Basin is not clear. A: Model 1, basin is filled with mare basalt. B: Model 2, a layered mafic pluton either survived or postdated the Nubium Basin formation. C: Model 3, a thick melt sheet from the Nubium Basin formation has been tapped by the Bullialdus impact.

(1979) and Cintala and Grieve (1993). This volume corresponds to a melt sheet 500 m to 2.5 km thick, depending on the lateral extent of the sheet. While cooling may have been very rapid near the surface, fractional crystallization might have occurred at greater depth, providing part or all of the stratigraphic sequence seen at Bullialdus. Even if the melt sheet did not differentiate, Bullialdus may have excavated part of a homogeneous melt layer to form either the central peaks or the walls. In fact, juxtaposition of melted and unmelted target rock at depth could explain the compositional boundary seen in the central peaks.

It is important to note that the origin of the SIC is still controversial, and its usefulness as an analog to lunar basins even more so. Warren (1993) has pointed out that the specific density contrasts predicted between the melt, the surrounding country rock, and major liquidus minerals could make both the formation of a thick melt sheet and its subsequent differentiation impossible on the moon. However, the present level of knowledge concerning multiring basin formation precludes any formal proof of either the occurrence or the lack of occurrence of fractional crystallization in melt sheets. Ultimately, it should be possible to make a strong case one way or the other through further observational studies, with data that provide the spectral as well as spatial resolution necessary to analyze in detail the compositional variations that occur across Bullialdus.

SUMMARY AND FUTURE DIRECTIONS

Spectral mixture modeling using multispectral images is rapidly becoming a widely used technique for studying lunar geology (e.g., Head et al., submitted for publication; Pinet et al. 1993). The results of the research presented here show that CCD data can be calibrated to reflectance and successfully used to map compositional boundaries, as has been done in terrestrial geology (e.g., Mustard and Pieters 1987). Using the compositional information derived from telescopic near-infrared spectra and a linear mixing model, a lithologic map and partial stratigraphic column have been assembled for Bullialdus, with compositional units that include anorthositic norite and noritic anorthosite at 6+ km beneath the surface, and gabbroic/basaltic material at shallower depths. This stratigraphic information was used to suggest three possible (and not mutually exclusive) models for the history of the Nubium Basin:

—The basin is filled with mare basalt to a greater depth than was previously assumed, and the basalt layer seen at the surface is a late-stage flow overlying a cratered surface consisting of earlier flows.

—A layered mafic intrusion was emplaced beneath or within the basin.

—A thick layer of impact melt could have formed as a result of the Nubium impact, and made up a part of the basin-filling materials.

As has been shown with this example, the material within a multiringed basin can be examined through smaller, later impact craters. The interaction of volcanism, plutonism, and impact lithologies such as melt and ejecta may be partly deconvolved through a careful examination of the spatial distribution of materials associated with craters as large as Bullialdus. Two of these, Models

2 and 3, would have implications for the evolution of the lunar crust, and specifically for the formation of Mg-suite rocks. While the true origins of the material excavated by Bullialdus cannot be determined with the CCD images used for this study, the three models offer testable alternatives given data with sufficient spectral and spatial resolution.

Many of the questions that remain may be addressed by similar studies of craters in settings comparable to Bullialdus (such as Copernicus; e.g., Pinet *et al.* 1993). In order to interpret the results of such studies, however, the way in which stratigraphy is inferred using impact craters must be more thoroughly modeled. The absolute depth of origin for central peaks is not understood, for example, and a shallower or deeper origin than the 6+ km that has been used in this paper would affect our interpretation of whether the Bullialdus central peak material came from within or beneath the Nubium Basin. A change in the estimate for the depth of the Nubium Basin itself would have the same effect.

The use of high spatial resolution, multispectral data provides a unique opportunity to test impact theories on lunar craters. As another example, the preimpact stratigraphic depths of wall and rim material are unconstrained except in a relative sense. These relationships have been studied in the terrestrial environment, both in the field and in the laboratory. However, terrestrial craters have been affected by weathering, and laboratory experiments cannot be tested on the scale of impacts the size of Bullialdus. Detailed compositional analyses of materials in and around craters like Bullialdus can provide excellent tests of theories relating the dimensions and morphology of impact craters and basins to their preimpact stratigraphy. High-spatial-resolution image data may provide detailed information on mixing dimensions and compositional boundaries that can be used to reexamine the predictions of laboratory and terrestrial studies for lunar craters.

ACKNOWLEDGMENTS

REFERENCES

ADAMS, J. B. 1974. Visible and near-infrared diffuse reflectance spectra of pyroxenes as applied to remote sensing of solid objects in the solar system. *J. Geophys. Res.* **79**, 4829–4836.

ADAMS, J. B., M. O. SMITH, AND A. R. GILLESPIE 1993. Imaging spectroscopy: Interpretation based on spectral mixture analysis. In *Remote Geochemical Analyses: Elemental and Mineralogical Com-*

position, (Pieters and Englert, Eds.). Cambridge Univ. Press, London/New York, in press.

ADAMS, J. B., M. O. SMITH, AND P. E. JOHNSON 1986. Spectral mixture modeling: A new analysis of rock and soil types at Viking Lander 1. *J. Geophys. Res.* **91**, 8113–8125.

BRATT, S. R., S. C. SOLOMON, J. W. HEAD, AND C. H. THURBER 1985. The deep structure of lunar basins: Implications for basin formation and modification. *J. Geophys. Res.* **90**(B4), 3049–3064.

CHEVREL, S., P. PINET, AND O. LESBRE 1991. Copernicus: Comparison and complementarity between telescopic multispectral solid-state imaging and reflectance spectra (abstract). In *Lunar and Planetary Science Conference XXII*, pp. 201–202.

CINTALA, M. J., AND R. A. F. GRIEVE 1993. Differential scaling: Implications for central structures in large lunar craters (abstract). In *Lunar and Planetary Science Conference XXIV*, pp. 291–292.

DEHON, R. A. 1977. Mare Humorum and Mare Nubium: Basalt thickness and basin forming history. In *Proceedings, Lunar Science Conference, 8th*, pp. 633–641.

DEHON, R. A. 1979. Thickness of the western mare basalts. In *Proceedings, Lunar Science Conference, 10th*, pp. 2935–2955.

ELVIDGE, C. D. 1988. Examination of the spectral features of vegetation in 1987 AVIRIS data. In *Proceedings, AVIRIS Perf. Eval. Workshop*, JPL Pub. 88-38, pp. 97–101.

GRIEVE, R. A. F., D. STÖFFLER, AND A. DEUTSCH 1991. The Sudbury structure: Controversial or misunderstood? *J. Geophys. Res.* **96**, 22,753–22,764.

HAPKE, B. 1981. Bidirectional reflectance spectroscopy. 1. Theory. *J. Geophys. Res.* **86**, 3039–3054.

HAWKE, B. R., P. G. LUCEY, AND J. F. BELL 1986. Spectral reflectance studies of Tycho Crater: Preliminary results (abstract). In *Lunar and Planetary Science XVII*, pp. 999–1000. Lunar Planet. Inst., Houston.

HAWKE, B. R., AND J. W. HEAD 1977. Impact melt on lunar crater rims. In *Impact and Explosion Cratering*, pp. 815–841.

HEAD, J. W., S. W. MURCHIE, J. F. MUSTARD, C. M. PIETERS, G. NEUKUM, A. MCEWEN, R. GREELEY, AND M. J. S. BELTON. Lunar impact basins: New data for the western limb and farside (Orientale and South Pole–Aitken Basins) from the first Galileo flyby. Submitted for publication.

HEAD, J. W. 1974. Orientale multi-ringed basin interior and implications for the petrogenesis of lunar highland samples. *Moon* **11**, 327–356.

HEAD, J. W. 1982. Lava flooding of ancient planetary crusts: Geometry, thickness, and volumes of flooded lunar basin impacts. *Moon Planets* **26**, 61–88.

HEAD, J. W., AND L. WILSON 1992. Lunar mare volcanism: Stratigraphy, eruption conditions, and the evolution of secondary crust. *Geochim. Cosmochim. Acta* **56**, 2155–2175.

JOHNSON, T. V., C. M. PIETERS, AND T. B. MCCORD 1973. Mare Humorum: An integrated study of spectral reflectivity. *Icarus* **19**, 224–229.

LANGE, M. A., AND T. J. AHRENS 1979. Impact melting early in lunar history. In *Proceedings Lunar Planetary Science Conference, 10th*, pp. 2707–2725.

LUCEY, P. G., B. C. BRUNO, AND B. R. HAWKE 1991. Preliminary results of imaging spectroscopy of the Humorum Basin Region of the Moon. In *Proceedings, Lunar and Planetary Science Conference 21*, pp. 391–403.

LUCEY, P. G., B. R. HAWKE, C. M. PIETERS, J. W. HEAD, AND T. B. MCCORD 1986. A compositional study of the Aristarchus region of the moon using near-infrared reflectance spectroscopy. In *Proceedings, Lunar and Planetary Science Conference, 16th, J. Geophys. Res.* **91**, D344–D354.

McGETCHIN, T. R., M. SETTLE, AND J. W. HEAD 1973. Radial thickness variation in impact crater ejecta: Implications for lunar basin deposits. *Earth Planet. Sci. Lett.* **20**, 226–236.

MELOSH, H. J. 1989. *Impact Cratering.* Oxford Univ. Press, New York.

MUSTARD, J. F., AND C. M. PIETERS 1987. Abundance and distribution of serpentinized ultramafic microbreccia in Moses Rock Dike: Quantitative application of mapping spectrometer data. *J. Geophys. Res.* **92**, 10,376–10,390.

MUSTARD, J. F., AND C. M. PIETERS 1989. Photometric phase functions of common geologic minerals and applications to quantitative analysis of mineral mixture reflectance spectra, *J. Geophys. Res.* **94**, 13,619–13,634.

NYQUIST, N. E., AND C. Y. SHIH 1992. The isotopic record of lunar volcanism. *Geochim. Cosmochim. Acta* **56**, 2113–2234.

PIETERS, C. M., J. W. HEAD, T. B. McCORD, J. B. ADAMS, AND S. ZISK 1975. Geochemical and geological units of mare humorum: Definition using remote sensing and lunar sample information. In *Proceedings, Lunar Science Conference, 6th,* pp. 2689–2710.

PIETERS, C. M., J. W. HEAD, J. M. SUNSHINE, E. FISCHER, S. L. MURCHIE, M. BELTON, A. McEWEN, L. GADDIS, R. GREELEY, G. NEUKUM, R. JAUMANN, AND H. HOFFMANN. Crustal diversity of the moon: Compositional analyses of Galileo SSI data. Submitted for publication.

PIETERS, C. M., AND D. E. WILHELMS 1985. Origin of olivine at Copernicus. In *Proceedings, Lunar Planetary Science Conference 15th, J. Geophys. Res.* **90**, C415–C420.

PIETERS, C. M. 1991. Bullialdus: Strengthening the case for lunar plutons. *Geophys. Res. Lett.* **18**, 2129–2132.

PIETERS, C. M. 1986. Composition of the lunar highland crust from near-infrared spectroscopy. *Rev. Geophys* **24**, 557–578.

PIETERS, C. M. 1993. Compositional diversity and stratigraphy of the lunar crust derived from reflectance spectroscopy. In *Remote Geochemical Analyses: Elemental and Mineralogical Composition* (Pieters and Englert, Eds.), pp. 309–336. Cambridge Univ. Press, London/New York.

PINET, P., S. CHEVREL, AND P. MARTIN 1993. Copernicus: A regional probe of the lunar interior. *Science* **206**, 797–801.

PINET, P., S. CHEVREL, AND P. MARTIN 1992. Detailed spectro-mixing analysis of Copernicus Crater from high resolution visible-near infrared imaging data (abstract). *Lunar and Planetary Science XXIII,* pp. 1075–1076.

RAEDEKE, L. D., AND I. S. McCALLUM 1980. A comparison of the fractionation trends in the lunar crust and the Stillwater Complex. In *Proceedings, Conference Lunar Highlands Crust* (J. J. Papike and R. B. Merrill, Eds.), pp. 133–153.

SABOL, D. E., J. B. ADAMS, AND M. O. SMITH 1992. Quantitative subpixel spectral detection of targets in multispectral images. *J. Geophys. Res.* **97**, 2659–2672.

SMITH, M. O., S. L. USTIN, J. B. ADAMS, AND A. R. GILLESPIE 1990. Vegetation in deserts. 1. A regional measure of abundance from multispectral images. *Remote Sensing Environment* **31**, 1–26.

STÖFFLER, D., H.-D. KNOLL, U. B. MARVIN, C. H. SIMONDS, AND P. H. WARREN 1980. Recommended classification and nomenclature of lunar highland rocks—a committee report. In *Proceedings, Conference Lunar Highlands Crust* (J. J. Papike and R. B. Merrill, Eds.), pp. 51–70.

SUNSHINE, J. M., C. M. PIETERS, AND J. W. HEAD. New evidence for compositional diversity at Marius Hills from Galileo multi-spectral imaging. Submitted for publication.

THURBER, C. H., AND S. C. SOLOMON 1978. An assessment of crustal thickness variations on the lunar near side: Models, uncertainties, and implications for crustal differentiation. In *Proceedings, Lunar Planetary Science Conference, 9th,* pp. 3481–3497.

TOMPKINS, S. T., J. F. MUSTARD, C. M. PIETERS, AND D. W. FORSYTH 1993. Objective determination of image end-members in spectral mixture analysis (abstract). In *Lunar Planetary Science XXIV,* pp. 1431–1432.

TOMPKINS, S., C. M. PIETERS, J. F. MUSTARD, AND P. PINET 1992. Distribution of the materials around the lunar crater Bullialdus: A spectral mixing analysis (abstract). In *Lunar Planetary Science XXIII,* pp. 1435–1436.

TRASK, N. J., AND S. R. TITLEY 1966. *Geologic Map of the Pitatus Region of the Moon.*

WARREN, P. C., AND J. T. WASSON 1977. Pristine nonmare rocks and the nature of the lunar crusts. In *Proceedings, Lunar Planetary Science Conference, 8th,* pp. 2215–2235.

WARREN, P. C. 1993. Limits on differentiation of melt "sheets" from basin-scale lunar impacts (abstract). In *Lunar Planetary Science XXIV,* pp. 1481–1482.

WARREN, P. C. 1985. The magma ocean concept and lunar evolution. *Ann. Rev. Earth Planet. Sci.,* 13,201–13,240.

WALKER, D., J. LONGHI, AND J. F. HAYS 1975. Differentiation of a very thick magma body and implications for the source regions of mare basalts. In *Proceedings, Lunar Science Conference 6th,* pp. 1103–1120.

WILHELMS, D. E. 1987. *The Geologic History of the Moon.* USGS-PP No. 1348.

WOOD, J. A., J. S. DICKEY, JR., U. B. MARVIN, AND B. N. POWELL 1970. Lunar anorthosites and a geophysical model of the moon. In *Proceedings, Lunar Science Conference, 1st,* pp. 965–988.